Title

Evaluating Propeller-Wing Interactional Noise Predictions from a Medium-Fidelity Approach

Journal

Proceedings of the Sixth Decennial VFS Aeromechanics Specialists Conference, Santa Clara, California, Feb 2024

Authors

Ramsarran, Tyler
Brentner, Kenneth
Trembois, Nikos
et al.

Publication Date

2024-02-06

DOI

10.4050/sm-2024-tvf-5089

Evaluating Propeller-Wing Interactional Noise Predictions from a Medium-Fidelity Approach

Tyler Ramsarran
MS Student

Kenneth S. Brentner
Professor

Penn State University
University Park, Pennsylvania, USA

Nikos Trembois
PhD Student

Ethan Brown
PhD Student

Seongkyu Lee
Professor

University of California, Davis
Davis, California, USA

ABSTRACT

Propeller-wing interactions are a complex noise phenomenon and the noise prediction of these interactions is extremely relevant for the design and production of novel VTOL aircraft. This research provides a better understanding of these interactions from a medium-fidelity approach. The medium-fidelity approach can offer more rapid understanding of the acoustic impact of a design than high-fidelity approaches, but given the complexity of the propeller and wing flow interactions, the validity of acoustic predictions is of concern. This paper studies the noise directivity of multiple propeller-wing configurations with comparisons against experimental and high-fidelity CFD. The studies performed involve an isolated propeller, three wing positions in propeller-wing setups, and two cases where the wing-only and propeller and wing are placed at a 5-degree angle of attack. The results provided include per-source acoustic time pressure histories, in-plane SPL spectra, and stereographic projections of hemisphere array directivity. This research demonstrates that a medium-fidelity approach is capable of estimating propeller-wing interaction noise but with some discrepancies between experiment, medium-fidelity, and high-fidelity.

INTRODUCTION

Propeller-wing configurations are a source of complex noise relevant to the design and production of novel VTOL aircraft. Common propeller-wing configurations include tiltrotor and tiltwing designs, with applications to advanced air mobility (AAM) aircraft. One such example arises in the development of aircraft using distributed electric propulsion, in which there are many propellers placed on wings to provide lift. As these designs become more feasible with today's technological advancements, the current understanding of the acoustic implications of such designs requires further study.

Some of the current work to understand the fundamental causes of the acoustic implications appears in studies about the aerodynamic interactions that occur between propellers mounted to wings. In the case of tiltrotor aircraft, Lim (Ref. 1) studied the XV-15 rotor on a full-span wing when the aircraft is cruising at 220 knots. Lim identified that various interactions occur between the rotors and the airframe when in this configuration. These effects include the wing circulation and upwash affecting the inflow of the proprotor, the proprotor downwash periodically exciting lift on the wing, and the blade root and nacelle vortex convecting past the wing. Through high-fidelity simulation, Lim was able to identify and separate the multiple aerodynamic interactions between the proprotor and wing to identify the changes in blade loading when the proprotor is isolated and when the wing is introduced.

Similar work was continued on the study of the XV-15 tiltrotor by Zhang et al. (Ref. 2). This work expands upon the work from Lim on the study of proprotor-wing aerodynamic interactions through a medium-fidelity analysis with RCAS and PSU-WOPWOP. Zhang et al. modeled the XV-15 rotor and full-span wing to focus on the interactions between the proprotor and wing, excluding those from the nacelle, fuselage, and empennage. This work validates that there are significant loading differences when the tiltrotor operates in the presence of a wing. Additionally, this work begins studying the acoustic impact of interactional aerodynamics by providing the noise directivity of the tiltrotor; however, this study did not include the wing as a noise source in the prediction.

From an experimental approach, Zawodny, Boyd, and Nark prepared a propeller-wing configuration in the NASA Langley Low Speed Aeroacoustic Wind Tunnel (LSAWT) (Ref. 3). Their experiment places the leading edge of a wing at various locations rearward and upward relative to the propeller hub. In doing so, they studied some of the aerodynamic performance changes, such as the change in propeller thrust, wing pressure

Presented at the Vertical Flight Society's 6th Decennial Aeromechanics Specialists' Conference, Santa Clara, CA, Feb. 6-8, 2024.

coefficient, and axial Mach number upstream of the propeller as the wing is placed in different positions. Furthermore, they provided more focus on the aeroacoustic results from both the wing and the propeller by using a linear array of 28 microphones ahead of and behind the setup to study the directivity of the noise. This provided a new understanding that there are significant changes in noise caused by the aerodynamic interactions between a propeller and wing.

Recently, research by Trembois et al. (Ref. 4) furthers the study of aeroacoustic interactions by expanding upon the work by Zawodny et al. Through high-fidelity analysis with NASA OVERFLOW, this research considers a computational setup of the experimental case and offers more detail about the aerodynamic and aeroacoustic interactions. Specifically, it studies the aeroacoustic phenomenon from an individual source perspective, including the propeller and wing as unique noise sources. These sources are also split into thickness and loading tonal noise sources to check how each noise source changes as the aerodynamic configuration changes.

This paper intends to expand upon the research by Trembois et al. to focus on the medium-fidelity approach to studying the aeroacoustic interactions in propeller-wing configurations. The medium-fidelity analysis is critical for acoustic prediction since it offers a more rapid study of configurations than high-fidelity approaches, saving the cost and time of preparing and running high-fidelity simulations. Moreover, these faster analyses can be useful for understanding the acoustic impact of future VTOL aircraft during the design process. For these cases, the propeller and wing are tested at 0° and +5° angles of attack relative to axial flight. It is worthwhile noting that this paper only focuses on tonal noise, not including broadband noise, even though broadband noise can also be an important noise source for AAM aircraft (Refs. 5–7).

Figure 1: Experimental propeller-wing setup (Ref. 3). Note, the orientation of the wing in relationship to the propeller is inverted in the experiment as compared to Fig. 2.

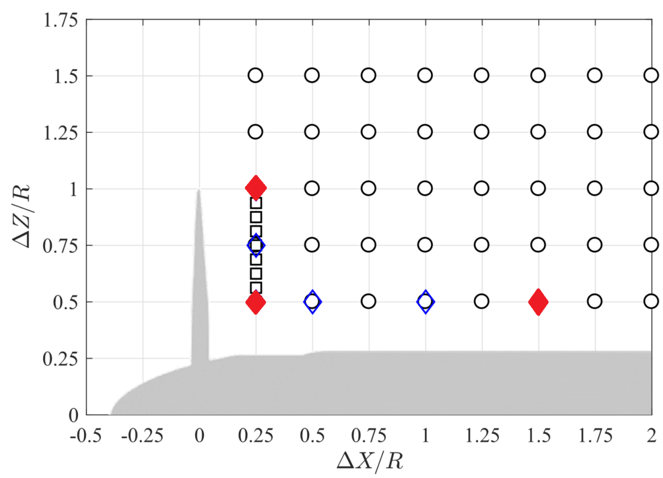

Figure 2: Wing leading edge location relative to the propeller hub, i.e., $X/R = 0.0$, $Z/R = 0.0$ (Ref. 3). The red diamonds indicate the wing locations used for the RCAS predictions in this paper.

TECHNICAL APPROACH

To study the propeller-wing interactional noise phenomenon, this research references a recent experiment at NASA Langley Research Center reported by Zawodny et al. (Ref. 3) with a propeller-wing setup with a 16x11 in., diameter by pitch, Mejzlik 3-bladed propeller and an NACA $63_2 - 215$ MOD B airfoil for the wing. The setup is tested for aerodynamic performance and acoustic measurements for a 3-bladed propeller on a wing in the Langley Low Speed Aeroacoustic Wind Tunnel (Fig. 1). To test for different propeller-wing configurations, the propeller position is held constant while the wing leading edge is moved to different positions. The leading edge positions varied between 0.5 and 1.5 propeller radii above the propeller and between 0.25 and 2.0 propeller radii behind the propeller, as shown in Fig. 2 (from Ref. 3).

RCAS Model

To simulate this setup with a medium-fidelity computation, the Rotorcraft Comprehensive Analysis System (RCAS) is selected (Ref. 8). For reference, "The Rotorcraft Comprehensive Analysis System (RCAS) is a comprehensive analysis developed by the U.S. Army to provide state-of-the-art rotorcraft modeling and analysis technology for Government, industry, and academia. It is a multi-disciplinary software system capable of detailed modeling a wide range of rotorcraft configurations operating in hover, forward flight, and maneuvering flight to predict performance, loads, vibration, flight dynamics, and aeroelastic stability (Ref. 8). Additionally, RCAS is a widely-used software tool that offers a medium level of fidelity for more rapid prototyping of designs than CFD or experimental approaches. As such, it may not capture the same detail as higher fidelity approaches. Still, RCAS remains an appropriate medium-fidelity tool for studying propeller-wing interactions.

The propeller and wing are considered rigid in their structural models. While it is possible to enable structural deformation of the propeller and wing, the rigid models are selected for simplicity. To determine the propeller location, it is attached by a rigid connection that extends forward from the

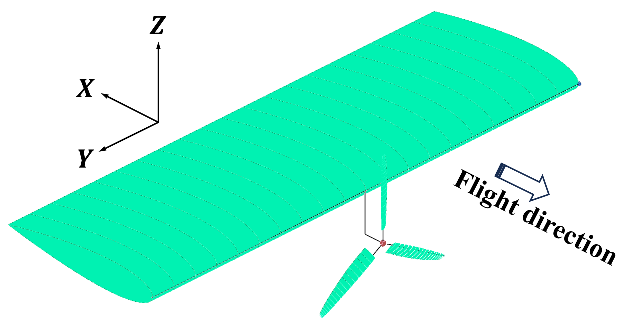

Figure 3: RCAS propeller and wing geometry with wing at $\Delta X/R = 0.25$, $\Delta Z/R = 0.5$.

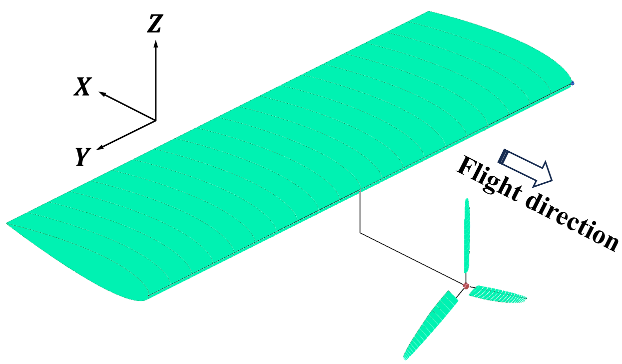

Figure 4: RCAS propeller and wing geometry with wing at $\Delta X/R = 1.5$, $\Delta Z/R = 0.5$.

leading edge of the wing (see Figs. 3 and 4). This connection is purely structural and does not affect the aerodynamic calculation. Additionally, this model does not include the nacelle. The propeller is designed with a collective node to allow for adjusting the pitch of all blades. Adjusting the collective in this model allows for matching the thrust coefficient of the experiment for the acoustic predictions.

The aerodynamic model attempts to match the original test case as well as possible. To do so, it specifies 7 airfoils along the span of each propeller blade. The airfoil geometry is extracted from a CAD model of the Mejzlik 16x11 propeller and smoothed to remove surface abnormalities and provide a sharp trailing edge. These seven airfoils are each simulated using C81gen to generate aerodynamic tables of lift, drag, and moment coefficients in C81 format. C81gen is a wrapper for ARC2D which prepares 2D grids for airfoil simulation (Refs. 9,10). ARC2D is a Navier-Stokes CFD solver from NASA Ames Research Center that solves Reynolds-averaged Navier-Stokes equations for 2D compressible flow (Ref. 11). Preparing the 2D airfoil grids in C81gen and running ARC2D for 2D compressible flow allowed for generating aerodynamic coefficient lookup tables for each spanwise section at the relevant angles of attack, Reynolds numbers, and Mach numbers. RCAS then uses these lookup tables to compute the inflow of the propeller and export the periodic loading from the propeller and wing. Furthermore, the airfoil chord and twist are determined from the CAD model. These are provided in 21

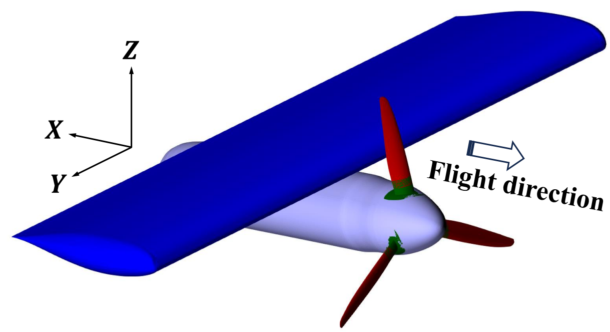

Figure 5: CFD near-body grids with the wing at $\Delta X/R = 0.25$, $\Delta Z/R = 0.5$.

spanwise segments with cosine spacing in the radial direction to ensure there is sufficient resolution to model the original propeller. The wing from the experiment is a $63_2 - 215$ MOD B airfoil, so C81gen and ARC2D have also been used to generate aerodynamic coefficient lookup tables of the wing for the simulation.

However, an important limitation of this modeling approach is that in RCAS the wing is modeled as a lifting line, rather than a lifting panel. This is a limitation of RCAS and results in only a spanwise distribution of loading on the wing, rather than a 2-dimensional loading across both the span and chord of the wing. It is expected this may cause differences between the medium- and high-fidelity loading and loading noise generated by the wing.

The inflow model used in RCAS for this case is a Viscous Vortex Particle Method (VVPM). VVPM is selected because it is an inflow model capable of simulating the interactional effects between a propeller and wing. This is not an effect that could be studied by the prescribed or free-wake methods available in RCAS (Ref. 4).

CFD Model

NASA OVERFLOW is selected for the high-fidelity model. OVERFLOW is a CFD tool that solves unsteady compressible Reynolds-averaged Navier-Stokes equations. OVERFLOW has been extensively applied to predict the aerodynamics and aeroacoustics of rotating blades including coaxial rotors (Refs. 12–14), side-by-side rotors (Refs. 15, 16), and quadrotors (Ref. 17). For this model, the CFD mesh is modeled with curvilinear overset grids. The near-body grids are composed of three unique geometries: the propeller blades, the wing, and the nacelle as shown in Fig. 5. The propeller and wing are both modeled with O-type grid topology. The spinner is not modeled, instead the blade grids slide along the nacelle surface grids. The grids were created with Chimera Grid Tools (Refs. 18, 19) and UCD-BladeGenerator (Ref. 20).

The propeller and wing grids are created using 250 chordwise points, 150 spanwise points, and 65 points off the surface. The chordwise spacing for the blade and wing grids is 0.05% and 0.02% local chord spacing at the leading and trailing edge. The gap at the tip of the blades and wing is closed with a cap grid. The domains of the blade grids are connected to the nacelle via a collar mesh. The reference chord, c_{ref}, is defined as the blade chord length where $r/R = 0.75$, which is 1.2 inches. All near-body grids grow from a volume-wise spacing of y+ = 0.9 at the surface to 10% c_{ref}. This matches the finest off-body grid spacing, which is adjacent to the near-body grids. The off-body grids are coarsened in 8 steps to form a cube with sides that are 20 times the length of the blade radius, doubling in size each coarsening. Six revolutions are required to converge the CFD solution. Each time step uses 20 subiterations and advances the blade one-quarter of a degree.

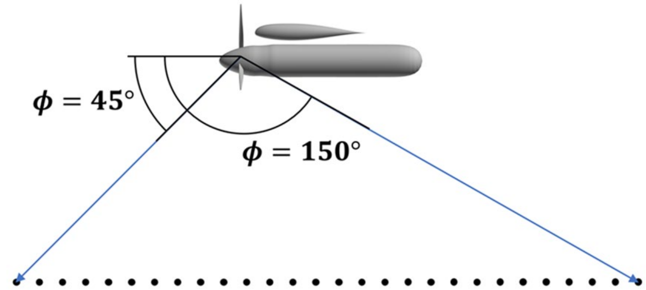

Figure 6: Side view of the microphone array with wing at $\Delta X/R = 0.25,\ \Delta Z/R = 0.5$ (Ref. 4).

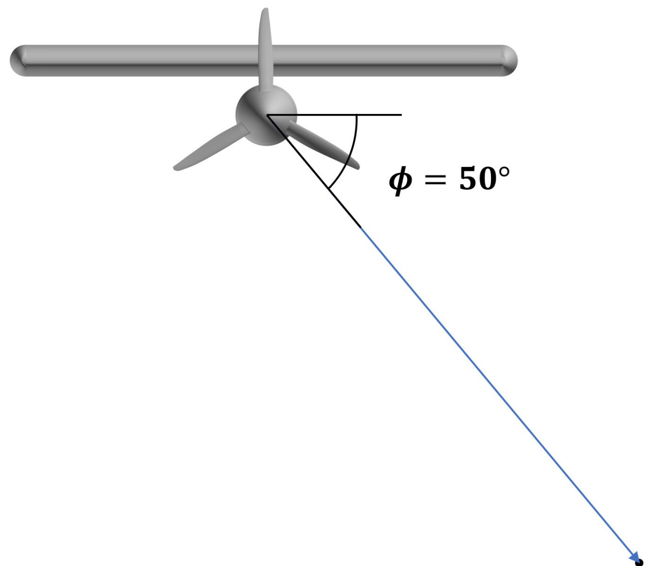

Figure 7: Front view of the microphone array with wing at $\Delta X/R = 0.25,\ \Delta Z/R = 0.5$ (Ref. 4).

Aeroacoustic Model

PSU-WOPWOP (Refs. 21–24) is used to calculate the tonal acoustic predictions for the simulated cases. It is a Ffowcs Williams−Hawkings solver that uses an implementation of Farassat's Formulation 1A (Refs. 25,26) to calculate the thickness and loading noise of these cases. To calculate the tonal thickness noise, PSU-WOPWOP requires the surface geometry of the test case. To calculate the tonal loading noise, PSU-WOPWOP requires force vectors acting on the geometry of the test case. Consequently, the surface geometry and loading force vectors for PSU-WOPWOP must be generated by an external analysis. Acoustic scattering by the wing has not been considered in any of the noise computations.

In this work, RCAS computes the information needed by PSU-WOPWOP. The coupling between RCAS and PSU-WOPWOP originates from the work by Sharma, Cole, and Brentner in Ref. 27. The coupling uses the RCAS outputs for the propeller to generate the required PSU-WOPWOP loading input. This work extends the coupling program by enabling the conversion of the RCAS wing outputs to allow for PSU-WOPWOP loading predictions on the wing. This updated system enabled RCAS to provide the aeroacoustic model with the required loading files for acoustic prediction. The required geometry files come from a CAD model of the propeller, as used in the CFD calculations.

In PSU-WOPWOP, a microphone array is prepared to match the setup used in the experiment. Accordingly, the array is a line of 28 microphones placed between elevation angles, $\phi = 45°$ and $150°$, shown in Fig. 6. They are also placed at a horizontal offset of $\theta = 50°$ (Fig. 7) to match the experiment. The radial distance to the nearest microphone in the array is 3.5 m. This is the nearest in-plane observer at $\phi = 93°$. For each observer of the array, PSU-WOPWOP is set up to calculate the acoustic pressure. This permits the calculation of noise spectra through Sound Pressure Level (SPL) for the various propeller-wing configurations, as well as comparisons of the noise directivity through SPL of the first Blade Passage Frequency (BPF) at various elevation angles, ϕ.

RESULTS

The RCAS model of the 16x11 3-bladed propeller is complete and demonstrates reasonable performance characteristics as compared to the experimental results. The performance of the propeller-wing model with the leading edge of the wing placed at 0.25 radii behind and 0.5 radii above the propeller hub is provided in Table 1. This case trims the collective pitch to match the thrust coefficient of the experiment results to ensure a fair comparison of the BPF SPL across the test cases. Upon trimming, the case applies a 0.59° collective pitch to the propeller. The trim procedure successfully matches the experimental thrust coefficient. Similarly, the comparison validates that it matches the blade tip Mach number, freestream Mach

Table 1: Mejzlik 16x11, 3-bladed propeller operating parameters with a wing installed in the nearest position, $\Delta X/R = 0.25,\ \Delta Z/R = 0.5$.

	Exp	Comp	% Error
Tip Mach number	0.361	0.361	-
Freestream Mach number	0.068	0.068	specified
Advance Ratio (J)	0.592	0.592	-
Thrust Coefficient (C_T)	0.0948	0.0948	target
Power Coefficient (C_P)	0.0128	0.0117	8.40
RPM	6000	6000	specified
Collective Pitch (deg)	0.0	0.59	-
Speed of sound (82.9F) (ft/s)	1141.7	1141.7	-

number, and therefore advance ratio well. Once RCAS trims the model to the desired thrust, the predicted power coefficient is lower than the experiment by an error of 8.40%.

A Note About the RCAS Loading Predictions

During the final assembly of this paper, an error was found in the wing loading in the RCAS setup. When that error was corrected, the RCAS loading for the wing was much higher (approximately 50 times the loading predicted by the CFD for the wing) even though the propeller loading predicted by RCAS was at the expected levels. Analysis of the results, and many separate checks, confirmed that the problem was only for the wing results, and it appeared to be only a scale factor. The source of this error was not determined in time for this paper, but the magnitude of the error was approximately the same as the ratio of the wing to propeller area (all three blades). Hence, the wing loading was reduced by a scale factor of 1/39.3 in the RCAS computations including the wing. It is not claimed that this is the source of the error, but the scaling was used to produce representative results for the paper.

In-Plane Acoustic Predictions

Acoustic predictions are provided below for three configurations. One configuration tests only the propeller for confirmation that the model is set up correctly. The latter two configurations test for two propeller-wing positions. The first propeller-wing position places the leading edge of the wing a quarter of the propeller's radius downstream of the propeller, and half of the propeller radius above the propeller axis of rotation. This is denoted as $\Delta X/R = 0.25$, $\Delta Z/R = 0.5$. The second propeller-wing position places the leading edge of the wing 1.5 propeller radii downstream and 0.5 propeller radii above the propeller. This is denoted as $\Delta X/R = 1.5$, $\Delta Z/R = 0.5$.

For the isolated propeller configuration, results are provided for a single, in-plane observer ($\phi = 93°$) in Figs. 8 and 9. Figure 8 shows the acoustic pressure recorded by the observer over one revolution. The three periods result because each blade passes by the observer during one revolution of the propeller. Figure 9 shows the SPL spectrum from this acoustic pressure for the in-plane observer. In Fig. 9 the SPL predictions based on the RCAS medium-fidelity and the OVERFLOW high-fidelity airloads are compared with the experiment. This spectrum shows that the SPL at the first BPF (300 Hz) and second BPF (600 Hz) match very well across the three datasets. The results from RCAS and OVERFLOW loading for the first BPF is 71 dB while the experiment is 68 dB. For the second BPF, RCAS has an SPL of 51 dB, while OVERFLOW has 52 dB, and the experiment has 53 dB. These results for the isolated case demonstrate that the medium-fidelity approach is capable of matching experimental acoustic results of the first two BPF frequencies; however, the missing broadband noise differentiates the medium-fidelity result at other frequencies – particularly above the second BPF.

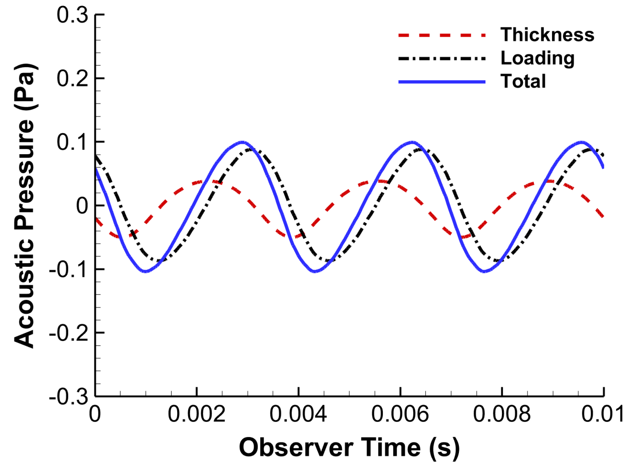

Figure 8: Predicted components and total acoustic pressure vs. time at the in-plane location with RCAS loading for the isolated propeller.

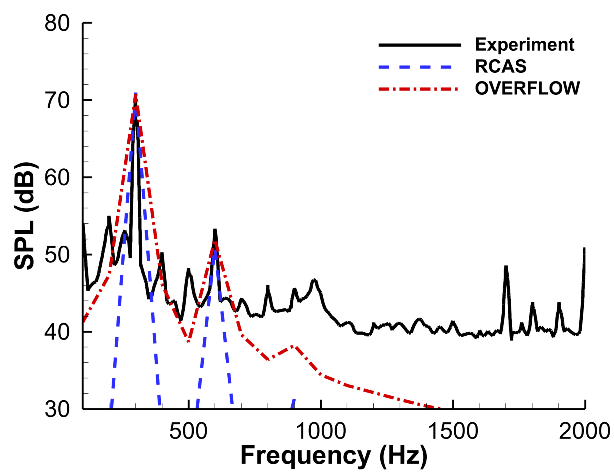

Figure 9: Comparison of measured and predicted SPL at the in-plane observer location for the isolated propeller using RCAS and OVERFLOW loading.

Results are provided for the baseline wing case, $\Delta X/R = 0.25$, $\Delta Z/R = 0.5$, for the same single, in-plane ($\phi = 93°$) observer in Figs. 10 and 11. Figure 10 shows the acoustic pressure at the observer over a single revolution for each noise source. The propeller thickness noise in Fig. 10 is identical to the isolated rotor in Fig. 8, which is expected. The propeller loading noise appears to be only slightly different from Fig. 8, which is due to the influence the wing has on the propeller blade loading. In addition to the propeller noise sources, there is an additional noise component due to the unsteady loading from the propeller on the wing, as shown in Fig. 10. The wing loading noise is a dominant source for this observer location and the RCAS-based loading yields a periodic result at the shaft rotation rate, but the individual pulses associated with each blade's wake passing over the wing are not identical. This behavior is not expected and not seen in the high-fidelity results (not shown). More research is needed to determine the source of this anomaly.

Figure 11 shows the corresponding SPL spectrum. Acoustic predictions for the medium-fidelity RCAS blade loads and high-fidelity OVERFLOW blade loads are compared, and the experimental results are shown for the first BPF. The acoustic predictions of the first BPF differ by approximately 8 dB between the RCAS and OVERFLOW blade loading cases, bracketing the experiment with medium-fidelity overpredicting and the high-fidelity result underpredicting the experimental value. For the second BPF in Fig. 11, the agreement between the two predictions is similar to the first (about 6 dB), but the predictions diverge for the third BPF and beyond, with the RCAS loading acoustic prediction substantially higher than the OVERFLOW loading acoustic prediction in this case. This may related to the anomalies already noted for the RCAS loading computations, but more investigation is needed to determine the full nature of any problem in the RCAS loading prediction.

Results for the in-plane observer ($\phi = 93°$) with wing position $\Delta X/R = 1.5$, $\Delta Z/R = 0.5$ are shown in Fig. 12, which compares the SPL spectrum for acoustic predictions using RCAS and OVERFLOW loading. A comparison of the first two BPFs reveals a small difference of only 2 dB between the two predictions. In this case, the SPL level of the third BPF for the RCAS case is significantly higher than the OVERFLOW case, which is consistent with the overprediction past the second BPF found in Fig. 11. It is speculated that the first two BPF agreements are better because the wing is farther away from the propeller.

SPL Directivity Predictions

Additional results consider the directivity of the noise across the linear microphone array of 28 microphones placed in the experiment (Ref. 3) and shown in Figs. 6 and 7. Since the first BPF is most relevant for noise, the SPL of the first BPF is plotted for $45° \le \phi \le 150°$ for comparison with the experiment. The directivity of the first BPF of predicted SPL for the isolated propeller with RCAS loading is shown in Fig. 13. This comparison shows that acoustic prediction with RCAS loading agrees quite well (with 2-3dB) across the range of $45° \le \phi \le 130°$, but is not as good for $\phi > 130°$. The directivity of the prediction seems shifted by $\Delta\phi \approx 5° - 10°$. The source of the directivity shift is not apparent at this time.

The noise directivity for the baseline wing case, $\Delta X/R = 0.25$, $\Delta Z/R = 0.5$, is shown in Fig. 14. The experimental measurements are compared with predictions based on RCAS and OVERFLOW loading. RCAS loading results in an underprediction of the SPL of the first BPF ahead of the propeller ($45° \le \phi \le 70°$) and then is higher than the experiment from $80° \le \phi \le 150°$. Furthermore, the directivity of the RCAS loading-based predictions does not agree very well with the experiment, but the maximum difference is still within 8 dB. In contrast, the OVERFLOW loading yields SPL predictions that are closer to the experiment for $45° \le \phi \le 120°$ but then are substantially too low for $\phi > 120°$. The source of this discrepancy is currently unknown.

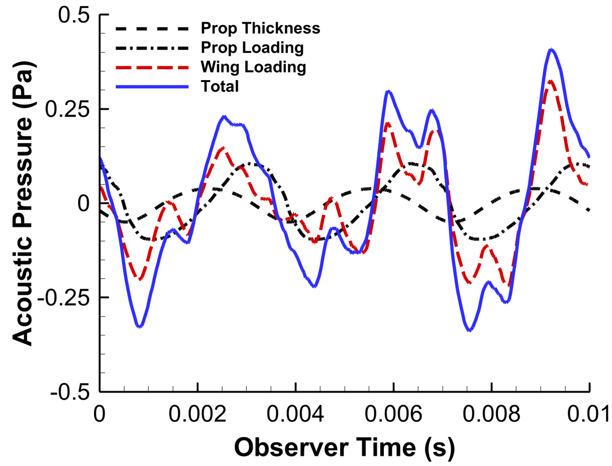

Figure 10: Predicted components of the propeller and wing acoustic pressure vs. time, using RCAS loading. The wing is located at $\Delta X/R = 0.25$, $\Delta Z/R = 0.5$.

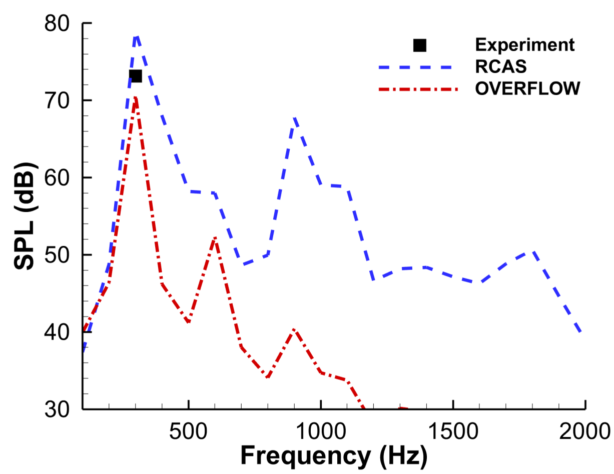

Figure 11: Measured and predicted SPL at the in-plane observer location using RCAS and OVERFLOW loading. The wing is located at $\Delta X/R = 0.25$, $\Delta Z/R = 0.5$.

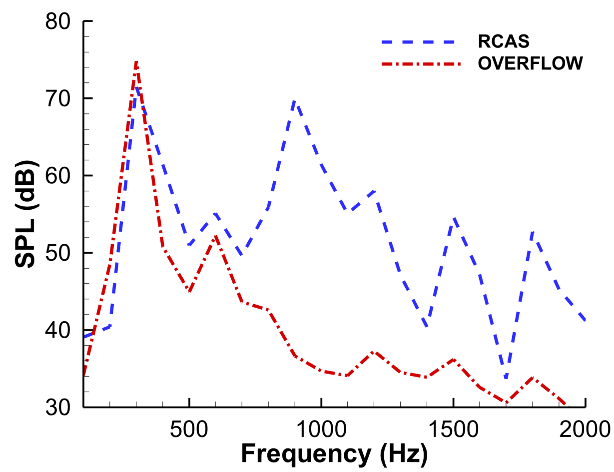

Figure 12: Comparison of predicted SPL at the in-plane observer location using RCAS and OVERFLOW loading. The wing is located $\Delta X/R = 1.5$, $\Delta Z/R = 0.5$.

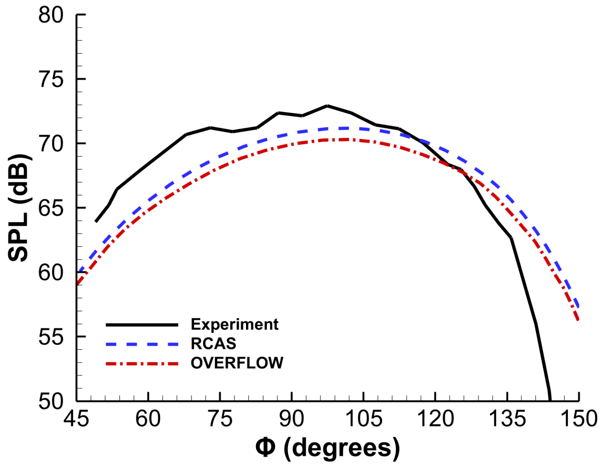

Figure 13: Measured and predicted directivity of the first BPF for the isolated propeller on the linear microphone array.

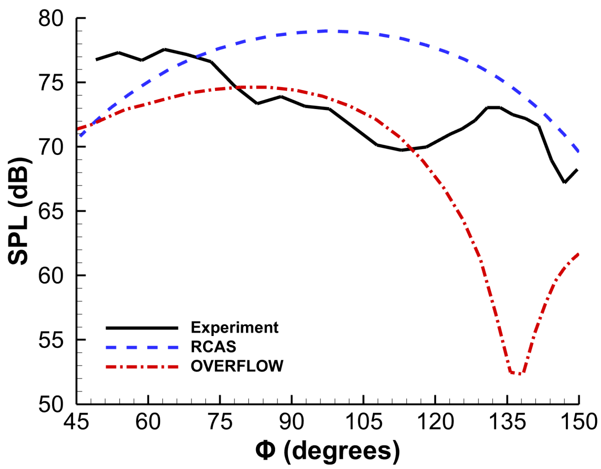

Figure 14: Measured and predicted directivity of the first BPF for the linear microphone array with the wing located at $\Delta X/R = 0.25$, $\Delta Z/R = 0.5$.

The noise directivity for the wing position $\Delta X/R = 1.5$, $\Delta Z/R = 0.5$ is shown in Fig. 15. The RCAS loading acoustic prediction is within 3 dB of the experiment for $45^\circ \leq \phi \leq 120^\circ$ and the directivity shape is also better than in Fig. 14. The OVERFLOW loading acoustic prediction agrees quite well with the experiment both in level and directivity shape. The improvement in both prediction directivities is consistent with Fig. 12 and is likely because the wing is farther from the propeller, thereby decreasing the significance of the propeller-wing interaction effect.

The noise directivity for the wing position $\Delta X/R = 0.25$, $\Delta Z/R = 1.0$ is shown in Fig. 16. In this wing location, both the RCAS and OVERFLOW loading-based acoustic predictions agree quite well with the experiment, although the RCAS results are not as close for $\phi > 120^\circ$. The good agreement for this wing location is also consistent with decreased propeller-wing interaction. Also, it should be pointed out that the OVERFLOW loading acoustic prediction matches the shape of the directivity for all angles $45^\circ \leq \phi \leq 150^\circ$.

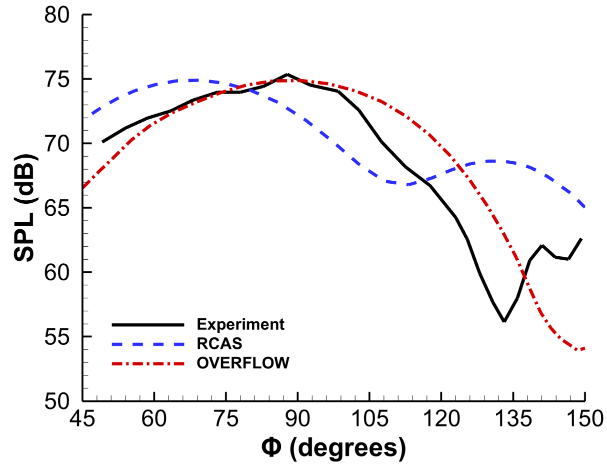

Figure 15: Measured and predicted directivity of the first BPF for the linear microphone array with the wing located at $\Delta X/R = 1.5$, $\Delta Z/R = 0.5$.

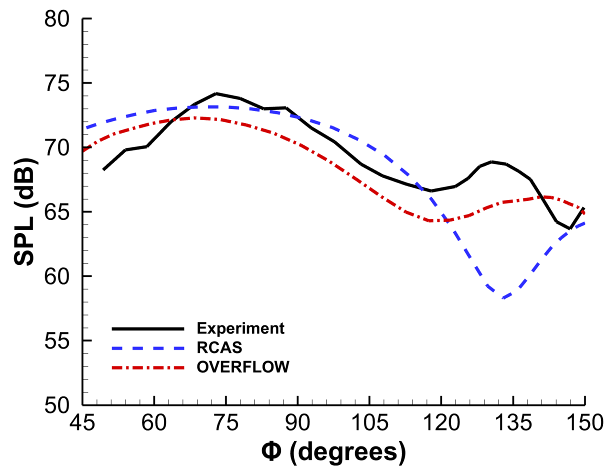

Figure 16: Measured and predicted directivity of the first BPF for the linear microphone array with the wing located at $\Delta X/R = 0.25$, $\Delta Z/R = 1.0$.

In the Zawodny et al. experiment (Ref. 3), the propeller-wing configuration was placed at $+5^\circ$ angle of attack in addition to the 0° angle of attack shown in all the previous predictions of this paper. The three angle of attack configurations predicted in this work are shown in Fig. 17 for the wing location $\Delta X/R = 0.25$, $\Delta Z/R = 0.5$. The 0° angle of attack case is shown in Fig. 17a for reference. The next configuration set the wing to $+5^\circ$ incidence relative to the freestream velocity, while the propeller was left at 0° incidence (Fig. 17b). The third configuration sets both the propeller and wing at $+5^\circ$ angle of attack relative to the freestream velocity (Fig. 17c).

The noise directivity along the linear array for the two different $+5^\circ$ angles of configuration was calculated for both RCAS and OVERFLOW loading, shown in Fig. 18. The noise levels were slightly higher when the propeller and wing were adjusted to $+5^\circ$ incidence as compared to when only the wing was inclined $+5^\circ$ for both RCAS and OVERFLOW loadings. But, as in the 0° angle of attack case, previously shown in Fig. 14, the directivity of the RCAS and OVERFLOW load-

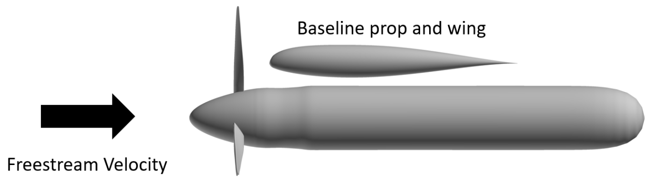

(a) Setup for the $\Delta X/R = 0.25,\ \Delta Z/R = 0.5$ wing position with no angle of attack.

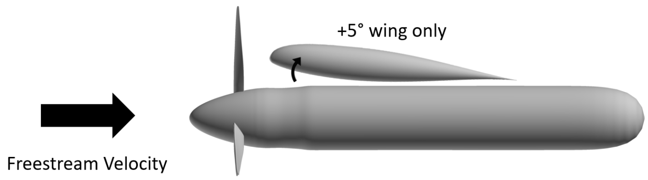

(b) Setup for the $\Delta X/R = 0.25,\ \Delta Z/R = 0.5$ wing position, for the +5° wing angle.

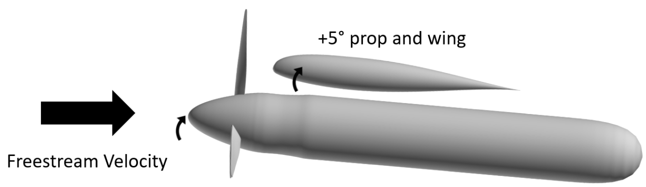

(c) Setup for the $\Delta X/R = 0.25,\ \Delta Z/R = 0.5$ wing position, for the +5° propeller and wing angle.

Figure 17: Geometry of propeller and wing for various angle of attack configurations.

ing cases are somewhat different. For the RCAS loading case, both the $+5^\circ$ angle of attack levels are lower than in Fig. 14 while for the high-fidelity case, the noise levels are somewhat higher in both $+5^\circ$ angle of attack cases. These changes cause the difference in acoustic predictions of the first BPF for RCAS and OVERFLOW loading along the linear array to be somewhat less than in the 0° angle of attack case. More study is needed to determine the reason why each of the cases behaves as they do.

Hemisphere Observer Acoustic Predictions

In addition to the comparisons of noise directivity on the linear microphone array, the noise predictions based on RCAS loading provided on a hemisphere observer below the propeller. This gives more information about how the noise changes in other directions at a constant distance. The noise predictions are made on a hemisphere with a radius of 13.4 propeller radii from the propeller hub, as shown in Fig. 19. The hemisphere has 21 equally spaced observers in the azimuth direction ($0^\circ \leq \psi \leq 360^\circ$) and 21 equally spaced observers in the elevation direction ($-90^\circ \leq \phi \leq 0^\circ$), where $\phi = 0^\circ$ is the $x-y$ plane and $\phi = -90^\circ$ is 13.4 propeller radii directly below the propeller hub. In Fig. 19, ψ is positive in the clockwise direction and ϕ is negative in the downward direction.

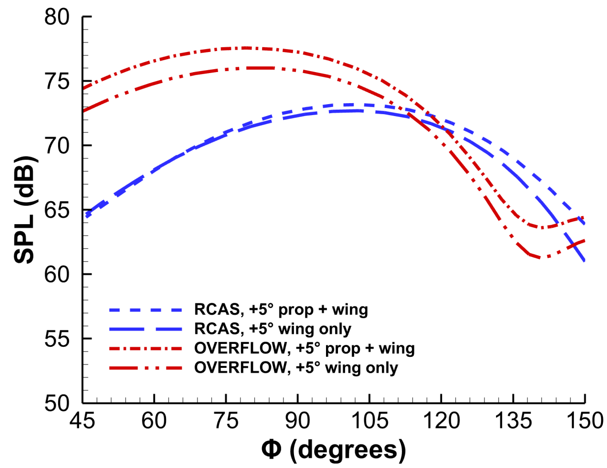

Figure 18: Measured and predicted directivity of the first BPF for the linear microphone array with the wing located at $\Delta X/R = 0.25,\ \Delta Z/R = 0.5$, for the +5° cases

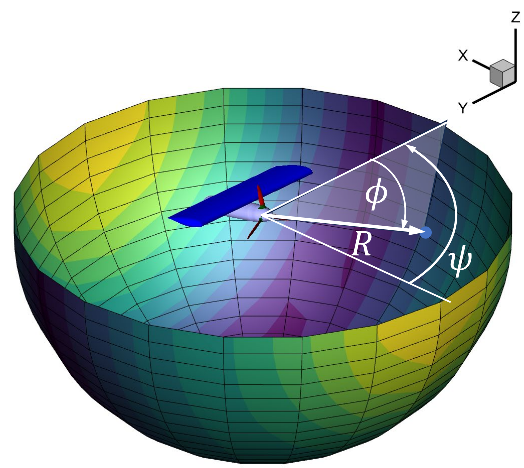

Figure 19: View of hemisphere of observers with positive azimuth ψ and negative elevation ϕ angles indicated. The sphere radius is 13.4 propeller radii R, $\psi = 0^\circ$ is directly in front of the propeller, $\phi = 0^\circ$ is in the $x-y$ plane, and $\phi = -90^\circ$ directly below the propeller.

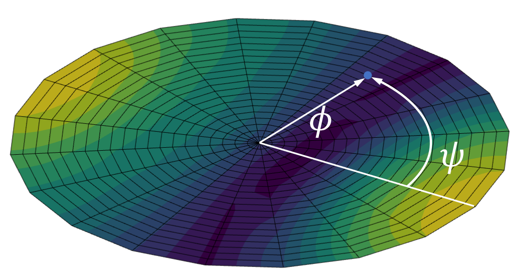

Figure 20: View of spherical projection of the hemisphere of observers in Fig. 19. Here $\phi = -90^\circ$ at the center of the circle and increase radially to the outer edge where $\phi = 0^\circ$.

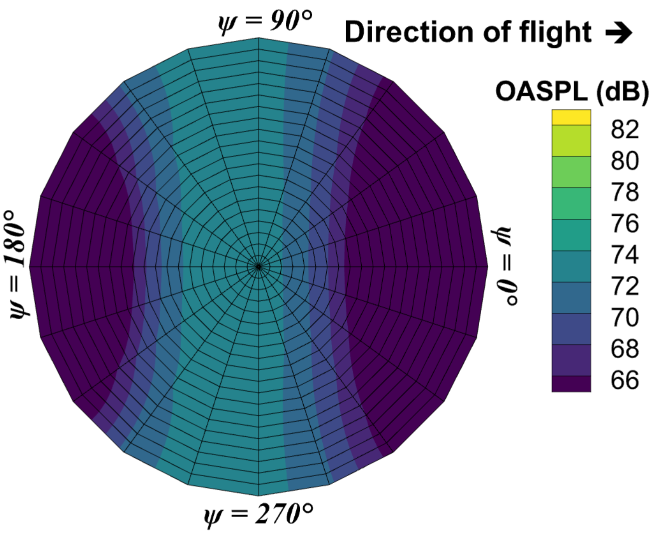

Figure 21: Stereographic projection of OASPL directivity for the isolated propeller with RCAS loading.

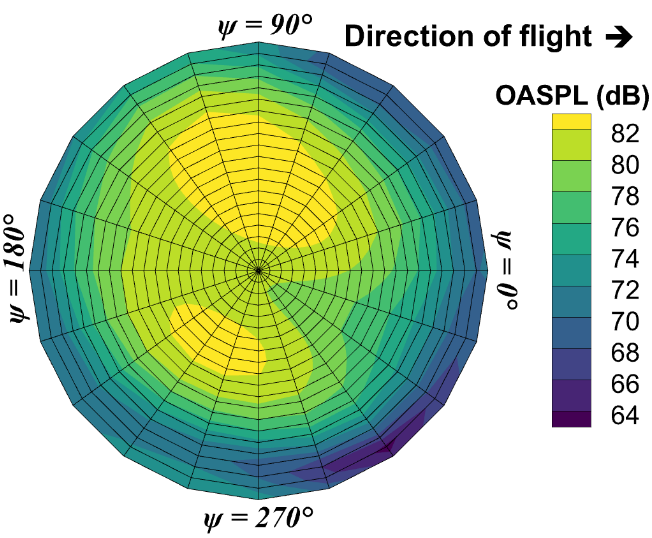

Figure 22: Stereographic projection of OASPL directivity for the baseline propeller-wing case with the wing located at $\Delta X = 0.25,\ \Delta Z = 0.5$ with RCAS loading.

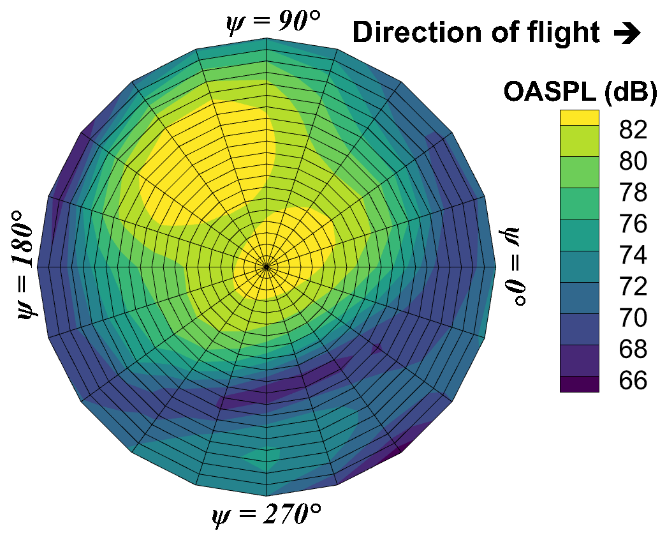

Figure 23: Stereographic projection of OASPL directivity for the baseline propeller-wing case with the wing located at $\Delta X = 0.25,\ \Delta Z = 0.5$ with OVERFLOW loading.

For visualization, these hemisphere observers are projected to a 2D surface through stereographic projection, as shown in Fig. 20. In Fig. 20, ψ and ϕ are shown in the positive directions, with $\psi = 0°$, $\phi = 0°$ directly in front of the propeller and $\phi = -90°$, the center, is directly below the propeller hub. The stereographic projection provides a good sense of the directivity on the sphere while providing a view of all elevation angles. Plotted on the projection are contours of the overall SPL (OASPL) recorded at each observer, integrated over one revolution of the propeller.

The first case considered is the OASPL prediction using RCAS loading for the isolated propeller case, Fig. 21. The isolated propeller case is relatively simple because the OASPL is the same at any azimuth angle around the propeller axis of rotation. This directivity is seen in Fig. 21 where the contour band along a line from $\psi = 90°$ to $\psi = 270°$ is the plane of the propeller rotation. This figure also shows there is some distortion from spherical projection as the observer position approaches $\phi = 0°$, which is the top of the hemisphere.

For the case where the leading edge of the wing is placed in the nearest proximity to the propeller ($\Delta X/R = 0.25$, $\Delta Z/R = 0.5$), shown in Fig. 22), there is an asymmetry of the OASPL contours due to the presence of the wing. There is a larger region of the maximum OASPL levels on the $\psi = 90°$ side of the hemisphere, where the propeller rotates upward toward the lower surface of the wing. On the $\psi = 270°$ side of the hemisphere, the propeller approaches the upper surface of the wing from the top as the propeller rotates downward. The region of maximum OASPL level is smaller and shifted rearward on this side of the hemisphere. This asymmetry is due to the loading noise generated by the wing due to the unsteady wing loading caused by the propeller wake.

When the wing is shifted rearward ($\Delta X/R = 1.5$, $\Delta Z/R = 0.5$), shown in Fig. 24, the region of highest OASPL levels has shifted rearward and is primarily below and behind the wing. This change is thought to be a result of the propeller wake interacting with the wing at a later time than in Fig. 22. The fact that the highest OASPL level is now behind and below the wing is speculated to be a result of the propeller wake going more below the wing. Future work will focus on verifying this hypothesis.

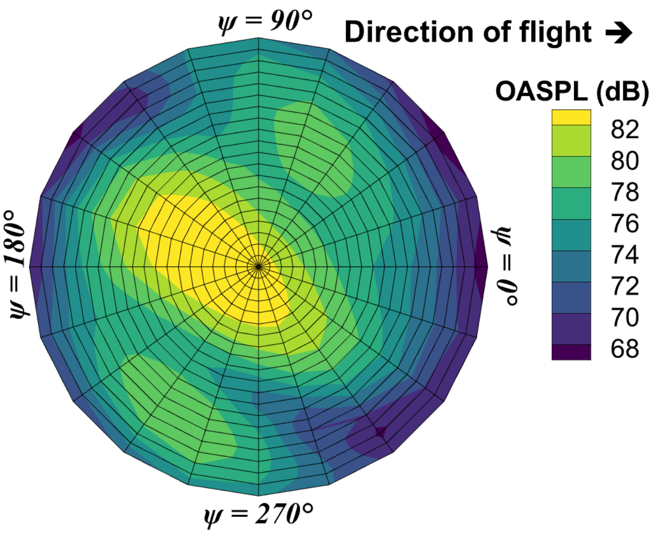

Figure 24: Stereographic projection of OASPL directivity for the propeller-wing case with the wing located at $\Delta X = 1.5,\ \Delta Z = 0.5$ with RCAS loading.

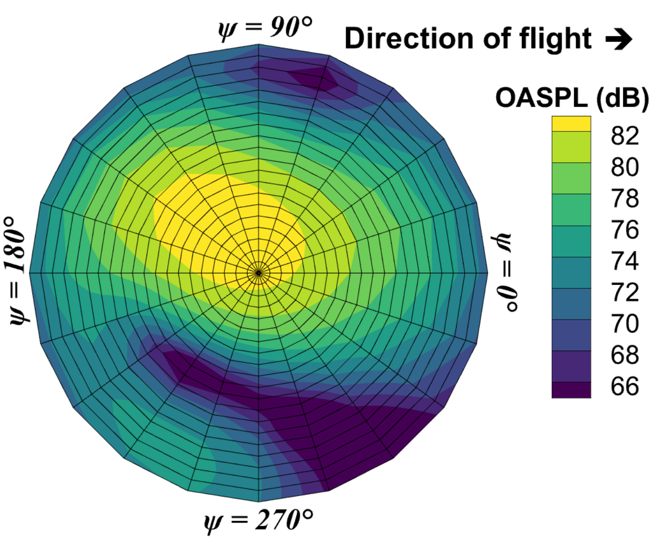

Figure 25: Stereographic projection of OASPL directivity for the propeller-wing case with the wing located at $\Delta X = 0.25,\ \Delta Z = 1.0$ with RCAS loading.

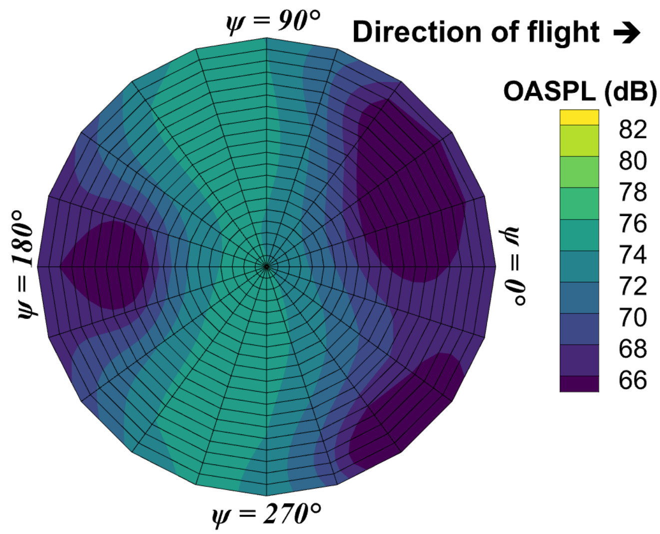

Figure 26: Stereographic projection of OASPL directivity for the case with only the wing adjusted to $+5^\circ$ angle of attack with RCAS loading.

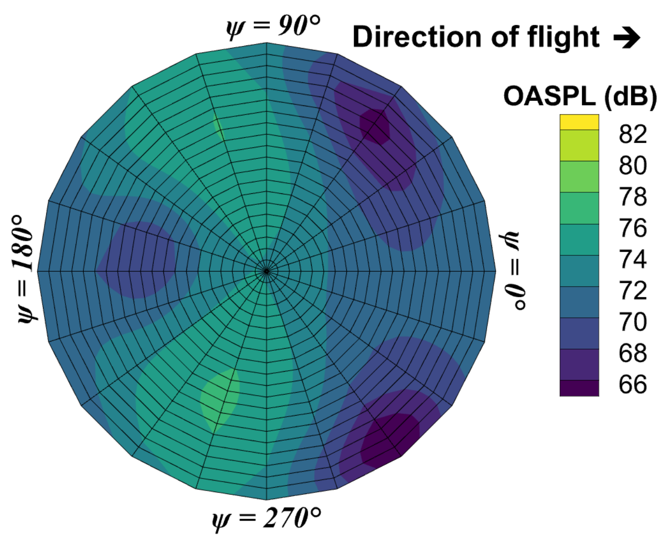

Figure 27: Stereographic projection of OASPL directivity for the case with the propeller and wing adjusted to $+5^\circ$ angle of attack with RCAS loading.

Next, when the wing is shifted upward ($\Delta X/R = 0.25,\ \Delta Z/R = 1.0$) instead of rearward, a similar change in directivity is seen when comparing Fig. 25 to Fig. 22 as is seen when comparing Fig. 24 to Fig. 22. The region of highest OASPL is very similar in Figs. 24 and 25, both below and behind the propeller and wing, but the noise away from that region is significantly lower. This change is likely because now the propeller wake is entirely below the wing and is only close to the wing at the top of the propeller wake.

Now, adjusting the wing case to have a $+5^\circ$ angle of attack relative to the freestream (Fig. 26), the noise becomes more symmetric about the axis of rotation and has OASPL levels comparable to the isolated propeller case in Fig. 21. The situation is similar when both the propeller and wing are set to $+5^\circ$ angle of attack, as shown in Fig. 27. Such low OASPL levels were not expected and are likely due to the wing not having the same levels as in the 0° angle of attack case. More study is required to understand these results, but it is likely that the computations in Figs. 26 and 27 are incorrect.

CONCLUDING REMARKS

This work has demonstrated that the acoustic interactions between a propeller and wing are complex, but they can be modeled by medium- and high-fidelity methods with varying degrees of accuracy. Through this study, multiple propeller-wing configurations were tested. These included three cases where the leading edge of the wing was placed close to the propeller, farther behind, and farther above the baseline wing location to compare acoustic predictions with experimental results. Through analysis of acoustic pressure time histories of the noise sources, SPL spectra of the in-plane noise, and linear and hemispherical arrays of microphones for the noise directivity, this research demonstrates that a medium-fidelity approach is capable of estimating propeller-wing interaction noise, but with some discrepancies between experiment, medium-fidelity, and high-fidelity. Predictions at both fidelity levels agreed very well for the isolated propeller, which is expected. When the interaction between the propeller and wing is included in the noise predictions the agreement between fidelity levels and experiment is often not as good. In general, the high-fidelity approach is more accurate, but at a substantial computation cost. Hence, there is still a desire to improve medium-fidelity tools to obtain reasonable predictions due to the much lower computational cost.

There is more work required to understand where the shortcomings of the medium-fidelity approach lie in this work. First, the anomaly in the wing loading computed by RCAS needs to be resolved and then the cases reassessed to determine if the the results are consistent with those presented in this paper. Also, further study is needed for the angle of attack cases to determine why the wing influence decreases so dramatically in the medium-fidelity approach. These two investigations may show that there is only one problem that presents itself in two different ways. The high-fidelity OVERFLOW results have already been used to help determine the problems with the RCAS computations, but more work is needed in this area. Once the algorithm and code problems are addressed, it will be possible to assess the difference between the approximations in RCAS as compared to the first principles approach used in CFD—and potentially improve the RCAS modeling.

Finally, while the noise directivity is often largely due to the tonal noise, as predicted in this paper, there remain differences identified in the higher harmonic noise between the computational analyses and the experiment. It is known from current practice and ongoing research that the higher harmonic noise is broadband noise, which was not included in the predictions from this paper. Development and application of broadband noise prediction tools will therefore aid in providing a more complete understanding of noise amplitudes and directivity, assisting in reducing the differences between computation and experiment.

ACKNOWLEDGMENTS

This research is funded by the Government under Cooperative Agreement No. W911W6-21-2-0002. The U.S. Government is authorized to reproduce and distribute reprints for Government purposes notwithstanding any copyright notation thereon. The views and conclusions contained in this document are those of the authors and should not be interpreted as representing the official policies or position, either expressed or implied, of the U.S. Army Combat Capabilities Development Command (DEVCOM), Aviation & Missile Center (AvMC), or the U.S. Government. Resources supporting this work were provided by the NASA High-End Computing (HEC) Program through the NASA Advanced Supercomputing (NAS) Division at Ames Research Center.

REFERENCES

1. Lim, J. W., "Fundamental Investigation of Proprotor and Wing Interactions in Tiltrotor Aircraft," Proceedings of the 75th Annual Forum of the Vertical Flight Society, Philadelphia, Pennsylvania, May 13–16, 2019.

2. Zhang, J., Brentner, K. S., and Smith, E. C., "Prediction of the Aerodynamic and Acoustic Impact of Propeller-Wing Interference," Proceedings of the Vertical Flight Society Technical Conference on Aeromechanics Design for Transformative Vertical Flight, San Jose, California, May 21–23, 2020.

3. Zawodny, N. S., Boyd, D. D., and Nark, D. M., "Aerodynamic and Acoustic Interactions Associated with Inboard Propeller-Wing Configurations," Proceedings of the AIAA Scitech Forum, Virtual, January 19–21, 2021, AIAA Paper 2021-0714.

4. Trembois, N., Brown, E., Lee, S., Ramsarran, T., and Brentner, K. S., "Prediction of Interactional Aerodynamic Noise of Propellers and Wing Using High-Fidelity CFD," Proceedings of the 79th Vertical Flight Society Annual Forum, West Palm Beach, FL, May 16–18, 2023.

5. Li, S. and Lee, S., "Prediction of Rotorcraft Broadband Trailing-Edge Noise and Parameter Sensitivity Study," *Journal of the American Helicopter Society*, Vol. 65, (4), October 2020, pp. 042006. doi: 10.4050/JAHS.65.042006

6. Li, S. and Lee, S., "Prediction of Urban Air Mobility Multi-Rotor VTOL Broadband Noise Using UCD-QuietFly," *Journal of the American Helicopter Society*, Vol. 66, (3), 2021, pp. 032004. doi: 10.4050/JAHS.66.032004

7. Lee, S., Ayton, L., Bertagnolio, F., Moreau, S., Chong, T. P., and Joseph, P., "Turbulent Boundary Layer Trailing-Edge Noise: Theory, Computation, Experiment, and Application," *Progress in Aerospace Sciences*, Vol. 126, (12), 2021, pp. 100737. doi: 10.1016/j.paerosci.2021.100737

8. Saberi, H., Hasbun, M., Hong, J., Yeo, H., and Ormiston, R., "Overview of RCAS Capabilities, Validations, and Rotorcraft Applications," Proceedings of the 71th Annual Forum of the American Helicopter Society, Virginia Beach, Virginia, May 5–7, 2015.

9. Strawn, R., Mayda, E. Q., and van Dam, C. P., "Automated CFD for Generation of Airfoil Performance Tables," Technical Report ARC-15649-1, November 2009.

10. Allen, L. D., Lim, J. W., Haehnel, R. B., and Dettwiller, I. D., "Rotor Blade Design Framework for Airfoil Shape Optimization with Performance Considerations," AIAA Scitech 2021 Forum, VIRTUAL EVENT, January 2021. doi: 10.2514/6.2021-0068

11. Pulliam, T., "Efficient Two-Dimensional Solution Methods for the Navier-Stokes Equations," *Tech Briefs*, Vol. 41, (10), October 2017.

12. Jia, Z. and Lee, S., “Impulsive Loading Noise of a Lift-Offset Coaxial Rotor in High-Speed Forward Flight,” *AIAA Journal*, Vol. 58, (2), 2020, pp. 687–701.
doi: 10.2514/1.J058295

13. Jia, Z., Lee, S., Sharma, K., and Brentner, K. S., “Aeroacoustic Analysis of a Lift-Offset Coaxial Rotor Using High-Fidelity CFD/CSD Loose Coupling Simulation,” *Journal of the American Helicopter Society*, Vol. 65, (1), 2020, pp. 012011.
doi: 10.4050/JAHS.65.012011

14. Jia, Z. and Lee, S., “Aerodynamically Induced Noise of a Lift-Offset Coaxial Rotor with Pitch Attitude in High-Speed Forward Flight,” *Journal of Sound and Vibration*, Vol. 491, 2021, pp. 115737.
doi: 10.1016/j.jsv.2020.115737

15. Jia, Z. and Lee, S., “High-Fidelity Computational Analysis on the Noise of a Side-by-Side Hybrid VTOL Aircraft,” *Journal of the American Helicopter Society*, Vol. 67, (2), 2022, pp. 022005.
doi: 10.4050/JAHS.67.022005

16. Sagaga, J. and Lee, S., “Performance, Aerodynamics, and Aeroacoustics of Side-by-Side Rotors Using High-Fidelity Computational Fluid Dynamics,” *AIAA Journal*, Vol. 61, (12), 2023, pp. 5429–5445.
doi: doi.org/10.2514/1.J062955

17. Jia, Z. and Lee, S., “Computational Study on Noise of Urban Air Mobility Quadrotor Aircraft,” *Journal of the American Helicopter Society*, Vol. 67, (1), 2022, pp. 012009.
doi: 10.4050/JAHS.67.012009

18. Chan, W., “Developments in Strategies and Software Tools for Overset Structured Grid Generation and Connectivity,” *20th AIAA Computational Fluid Dynamics Conference*, Fluid Dynamics and Co-located Conferences, American Institute of Aeronautics and Astronautics, June 2011, pp. 1–19.
doi: 10.2514/6.2011-3051

19. Chan, W., Gomez, R., Rogers, S., and Buning, P., “Best Practices in Overset Grid Generation,” *32nd AIAA Fluid Dynamics Conference and Exhibit*, Fluid Dynamics and Co-located Conferences, American Institute of Aeronautics and Astronautics, June 2002, pp. 1–23.
doi: 10.2514/6.2002-3191

20. Trembois, N., *Automatic Mesh Generation of Structured Overset Rotor Blades*, Master’s thesis, University of California, Davis, December 2020.

21. Brès, G. A., *Modeling the noise of arbitrary maneuvering rotorcraft: Analysis and implementation of the PSU-WOPWOP noise prediction code*, Master’s thesis, Department of Aerospace Engineering, The Pennsylvania State University, August 2002.

22. Perez, G., *Investigation of the influence of maneuver on rotorcraft noise*, Master’s thesis, Department of Aerospace Engineering, The Pennsylvania State University, 2002.

23. Brès, G. A., Brentner, K. S., Perez, G., and Jones, H. E., “Maneuvering rotorcraft noise prediction,” *Journal of Sound and Vibration*, Vol. 275, (3–5), August 2004, pp. 719–738.
doi: https://doi.org/10.1016/j.jsv.2003.07.005

24. Hennes, C., Lopes, L., Shirey, J., Cheng, R., Erwin, J., Lee, S., Goldman, B., Botre, M., Zachos, D., Gan, Z., Rau, R., Singh, N., Greenwood, E., and Brentner, K., *PSU-WOPWOP 3.5.0 User’s Guide*, July 2023.

25. Brentner, K. S. and Farassat, F., “Modeling aerodynamically generated sound of helicopter rotors,” *Progress in Aerospace Sciences*, Vol. 39, (2-3), 2003, pp. 83–120.

26. Farassat, F. and Succi, G., “The Prediction of Helicopter Discrete Frequency Noise,” *Vertica*, June 1983, pp. 309–320.

27. Sharma, K., Corle, E., Brentner, K., and Anusonti-Inthra, P., “Robust and automated coupling of RCAS and PSU-WOPWOP,” Proceedings of the AHS International Technical Meeting on Aeromechanics Design for Transformative Vertical Flight, January 2018.